

## Mobility Ratio as a Probe for Guiding Discovery of Thermoelectric Materials: The Case of Half-Heusler Phase $\text{ScNiSb}_{1-x}\text{Te}_x$

Kamil Ciesielski<sup>ID,\*</sup>, Izabela Wolańska<sup>ID</sup>, Karol Synoradzki<sup>ID</sup>, Damian Szymański<sup>ID</sup>, and Dariusz Kaczorowski<sup>ID</sup>

*Institute of Low Temperature and Structure Research, Polish Academy of Sciences, Okólna 2,  
Wrocław 50-422, Poland*



(Received 26 December 2020; revised 6 March 2021; accepted 23 March 2021; published 28 April 2021)

Analysis of bipolar thermal conductivity might be very useful in preliminary stages of thermoelectric materials discovery. Using its product—mobility ratio between electrons and holes—it is possible to choose the most promising compound from the series and pave the correct direction of doping. Current work presents positive verification of this approach for  $\text{ScNiSb}$ , which is anticipated to show superior mobility when tuned towards *n*-type behavior. In agreement with expectation, the mobility increases by an order of magnitude due to rising tellurium content in the  $\text{ScNiSb}_{1-x}\text{Te}_x$  series. The effect is most likely driven by change of the dominant charge carriers' scattering mechanism from ionized impurity influence to point defect and acoustic phonon interaction. Simultaneously, due to a highly anisotropic conduction band, the effective mass of the carriers rises towards the *n*-type regime. These two effects lead to an improved thermoelectric power factor of electron-doped samples, up to  $40 \mu\text{WK}^{-2} \text{cm}^{-1}$  at 740 K for  $\text{ScNiSb}_{0.85}\text{Te}_{0.15}$ . Based on this result, we suggest *n*-type doping for other rare-earth-based half-Heusler compounds. Representatives of this group exhibit the smallest lattice thermal conductivity in the pristine form among any half-Heusler thermoelectrics, and are anticipated to show comparably good electrical properties to  $\text{ScNiSb}$  due to their high mobility ratio in favor of electrons.

DOI: 10.1103/PhysRevApplied.15.044047

### I. INTRODUCTION

The ability to convert waste heat to electricity provided by thermoelectric (TE) materials is considered as one of the most promising solutions to the global demand of sustainable energy. Among many families of compounds considered for this purpose, half-Heusler (HH) phases appear to be the closest to large-scale application. They are ternary intermetallics with general formula  $MTX$ , where  $M$  stands for the early transition metal or RE element,  $T$  denotes late transition metal, and  $X$  corresponds to the *p*-electron element. Good thermoelectric performance of these compounds has been recognized for over 30 years [1–6]. Apart from the above, half-Heusler phases are also characterized by robust mechanical properties [7,8] and outstanding thermal stability [9], while keeping a rather low price [10]. The most extensively studied base composition, from a thermoelectric perspective, has historically been  $T^{IV}\text{NiSb}$  [1–4,11,12], where  $T^{IV}$  is transition metal from fourth group of the periodic table (Ti, Zr, Hf). Due to recent findings of superior TE performance in formerly unknown HH compositions, e.g.,  $\text{TaFeSb}$  [13],  $\text{ZrCoBi}$  [14], or  $\text{NbFeSb}$  [15], the attention of the scientific community is now turned

towards exploration of other poorly known subgroups of HH phases.

$\text{ScNiSb}$  belongs to the family of disordered RE-based HH phases [16–18]. Depending on the synthesis pathway, the compound is reported to maintain the stoichiometric composition [18] or exhibit a significant amount of nickel vacancies [17]. As a result of the detailed structural study, we uncover that  $\text{ScNiSb}$  [18] as well as other RE-bearing HH phases [16,19] exhibit unique additional defects. Namely, late transition metals atoms can be displaced from their nominal  $4c$  Wyckoff site ( $1/4,1/4,1/4$ ) to quarterly occupied  $16e$  ( $x,x,x$ ) position  $x$  ranging from 0.256 to 0.262.

Undoped  $\text{ScNiSb}$  is an intrinsic *p*-type conductor with rather light holes ( $m_{\text{eff}} \leq 1.5m_e$ , where  $m_{\text{eff}}$  stands for the effective mass of charge carrier) [16,20] and experimental energy gap of about 0.3 eV, somewhat depending on the crystallographic disorder [16,18,21,22]. Thermal conductivity of pristine  $\text{ScNiSb}$  is also largely affected by the presence of atomic defects and the microstructure of the specimen. At room temperature, it spans from  $4 \text{ Wm}^{-1}\text{K}^{-1}$  [22] to  $11 \text{ Wm}^{-1}\text{K}^{-1}$  [18], which is similar to the values obtained for other HH phases before nanostructurization:  $\text{ZrNiSn}$  ( $8 \text{ Wm}^{-1}\text{K}^{-1}$ ) [23],  $\text{VFeSb}$  ( $13 \text{ Wm}^{-1}\text{K}^{-1}$ ) [24],  $\text{ZrCoBi}$  ( $9 \text{ Wm}^{-1}\text{K}^{-1}$ ) [14].

\*k.ciesielski@intibs.pl

Conventionally, thermal conductivity is assumed to consist of a lattice part and a polar electronic term, that can be obtained from the Wiedemann-Franz law. However, above the temperature of minority carrier activation, one can also observe additional contribution from electron-hole pairs, known also as bipolar thermal conductivity (BTC). The phenomenon has been studied in semiconductors community for several decades [25–28]. From a thermoelectric perspective, the phenomenon is considered rather detrimental, as BTC increases total thermal conductivity; furthermore, the presence of minority carriers tends to decrease thermopower. This motivated development of different strategies to suppress BTC [29–34]. Furthermore, incorporation of BTC analysis of thermoelectric properties is shown to help explain the observed characteristic for half-Heusler phases [35–37] and other TE materials [38,39]. Recent joint experimental and theoretical work established that the effect is driven by the carrier mobility ratio in the intrinsic case and minority carrier partial electrical conductivity in the extrinsic regime [40].

Our recent analysis of bipolar thermal conductivity [19] uncovered a curious feature of ScNiSb, namely the ratio between mobility of electrons and holes in this compound attains a value as large as 8. This finding suggests that *n*-type doping for ScNiSb should result in substantially increased charge-carrier mobility, which in turn is expected to provide enhanced TE performance. In order to confront these predictions with experiment, we investigate the electron-doped series  $\text{ScNiSb}_{1-x}\text{Te}_x$ , and the results of this study are presented below. This work is a part of our large on-going project aimed at understanding TE and magnetic properties of RE-based HH phases [41–48].

## II. METHODS

The samples of  $\text{ScNiSb}_{1-x}\text{Te}_x$ ,  $x = 0, 0.03, 0.05, 0.10, 0.15$  are obtained by arc-melting elemental constituents (Sc dendrites 99.95 at.%, Ni rod 99.99 at.%, Sb lumps 99.999 at.%, Te lumps 99.999 at.%) in the copper heart under high-purity (5N) argon atmosphere. The total mass of each sample is about 2.5 g. Due to intensive evaporation of antimony during the synthesis, we add beforehand extra Sb in a quantity not exceeding 4% of the sample weight. In order to ensure proper mixing of the constituents, each specimen is flipped over and remelted 3 times. Subsequently, it is grounded in agate mortar under protective Ar atmosphere and melted 3 more times. Afterwards, the ingots are wrapped in Mo foil, sealed in quartz ampoules under vacuum and annealed at 800 °C for 3 weeks. The annealing process is finished by quenching the ampoules in cold water.

X-ray powder diffraction experiments are performed using an X'pert Pro PANalytical diffractometer (Cu K $\alpha$  radiation,  $\lambda = 0.154056$  nm, step = 0.001°). FullProf software [49] is employed for the Rietveld refinement.

The density of the samples is measured via the Archimedes method. SEM imaging and energy dispersive x-ray spectroscopy (EDS) is carried out on a FEI NovaNanoSEM 230 FE-scanning electron microscope equipped with Apollo *X* Silicon Drift Detector. For EDS analysis we use the following spectral lines: Sc-L $\alpha$ , Ni-K $\alpha$ , Sb-L $\alpha$ , Te-L $\alpha$ , while the beam-landing energy is equal to 20 keV. In order to ensure credibility of EDS analysis, we extend the data-collection time up to about 8.5 h per sample (128 frames, 200 s dwell time). The relative error of this method is 2% for the main elements and 5% for the minority elements. Low-temperature (2–300 K) Hall effect is measured using with Physical Property Measurement System (PPMS-9) equipped with a horizontal rotator. The carrier concentration ( $n$ ) is calculated from the formula  $n = 1/eR_H$ , where  $R_H$  is the Hall constant, while the carrier mobility ( $\mu_H$ ) is obtained from the equation  $\mu_H = \sigma|R_H|$ , where  $\sigma$  denotes the electrical conductivity. Electrical contacts are prepared on polished surfaces of the parallelepiped-shaped geometry specimens using epoxy and 50-μm diameter Ag wires. High-temperature (300–950 K) Seebeck coefficient ( $S$ ) and electrical resistivity ( $\rho$ ) are measured simultaneously employing Linseis LSR-3 device with platinum electrodes. Measurements of thermopower performed with temperature gradients 30, 40, and 50 K resulted in curves converging within the range of experimental error; for transparency in the paper we show only data gathered with 50-K gradient. The relative errors for  $\rho$  and  $S$  are 3% and 5%, respectively.

## III. RESULTS AND DISCUSSION

The XRD pattern measured for  $\text{ScNiSb}_{0.85}\text{Te}_{0.15}$  is displayed in Fig. 1, while the results for the other samples can be found within the Supplemental Material, Fig. S1 [50]. The refined lattice parameters ( $a$ ) and atomic occupancies are listed in Table I. A subtle decrease of  $a$  with a rising Te content in  $\text{ScNiSb}_{1-x}\text{Te}_x$  series is consistent with a smaller ionic radius of tellurium ( $r_{\text{Te}^{2-}} = 2.11$  Å) with respect to antimony ( $r_{\text{Sb}^{3-}} = 2.45$  Å) [51]. According to our previous study of ScNiSb with superior quality diffraction [18], Sc atoms resided at 4*a* (0,0,0) Wyckoff positions while Sb and Te are located at the 4*b* (1/2,1/2,1/2) site; Ni is assumed to reside on a quarterly occupied 16*e* (*x,x,x*) slot. To ensure validity of the Rietveld refinement with our laboratory XRD data, the Ni atomic coordinates as well as the thermal displacement parameters  $B_{\text{iso}}$  are fixed during the analysis, and values are acquired from Ref. [18]:  $x = 0.256$ ,  $B_{\text{iso}}(\text{Sc}) = 0.66$  Å<sup>2</sup>,  $B_{\text{iso}}(\text{Ni}) = 0.61$  Å<sup>2</sup>,  $B_{\text{iso}}(\text{Sb}/\text{Te}) = 0.59$  Å<sup>2</sup>.

Vacancies and antisite defects have a similar mathematical impact on Rietveld refinement. In the current study we decide to provide a general insight into disorder in  $\text{ScNiSb}_{1-x}\text{Te}_x$  series with the former approach due to its

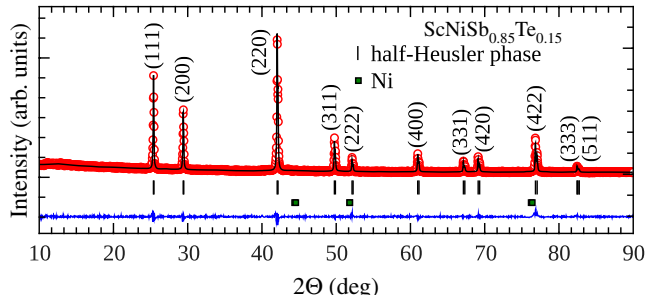


FIG. 1. Results of Rietveld refinement for the  $\text{ScNiSb}_{0.85}\text{Te}_{0.15}$  sample.

simplicity. In the first step, occupancies are relaxed separately on each atomic position. After finding vacancies on Sc and Ni sites, we normalize the composition to Sb+Te content; see Table I for the so-derived Sc and Ni occupancies. Similar atomic masses and roughly comparable ionic radii of  $\text{Sb}^{3-}$  and  $\text{Te}^{2-}$  hamper the precision of occupancy analysis on the  $4b$  site, so we fix the Sb/Te ratio to the nominal stoichiometry of the sample. We also perform the refinement with the possibility of Ni interstitials on the nominally empty  $4d$  ( $3/4, 3/4, 3/4$ ) site, which is reported for other HH phases [52,53]. The refinement resulted in either negative occupancies in the  $4d$  site, or a negligibly small ( $\leq 1.5\%$ ) amount of interstitial defects. No tendency is observed regarding the total number of defects detected by XRD analysis as a function of tellurium content. Scandium vacancies are most likely to be an acceptor defect, as the formal valence state of Sc in the studied material is  $3+$ , the whole compound having closed shells with  $\text{Sc}^{3+}\text{Ni}^0\text{Sb}^{3-}$ . This corroborates  $p$ -type conductivity observed for the undoped  $\text{ScNiSb}$  sample. The charge state of vacancies on the Ni site is rather hard to guess; *ab initio* defect calculations would be necessary to quantitatively answer this question. Our tentative intuition is, that in the majority of chemical conditions it would also form an acceptor defect, as vacancies on the Ni site are reported for  $\text{ScNiSb}$  previously in an even bigger amount, see Ref. [17], and undoped  $\text{ScNiSb}$  samples are always  $p$ -type conductors [16,18,21,22]. As a next step in our research, we plan to perform *ab initio* defect calculations for  $\text{ScNiSb}$  and

TABLE I. Lattice parameters and the refined atomic occupancies resultant from Rietveld refinement for the  $\text{ScNiSb}_{1-x}\text{Te}_x$  series.

Sample	$a$ (Å)	Sc occ. (%)	Ni occ. (%)
$\text{ScNiSb}$	6.0754(1)	98(1)	95(1)
$\text{ScNiSb}_{0.97}\text{Te}_{0.03}$	6.0740(1)	100	98.4(8)
$\text{ScNiSb}_{0.95}\text{Te}_{0.05}$	6.0728(2)	94(1)	94(1)
$\text{ScNiSb}_{0.90}\text{Te}_{0.10}$	6.0725(1)	94(1)	96.2(8)
$\text{ScNiSb}_{0.85}\text{Te}_{0.15}$	6.0712(2)	99(1)	99(1)

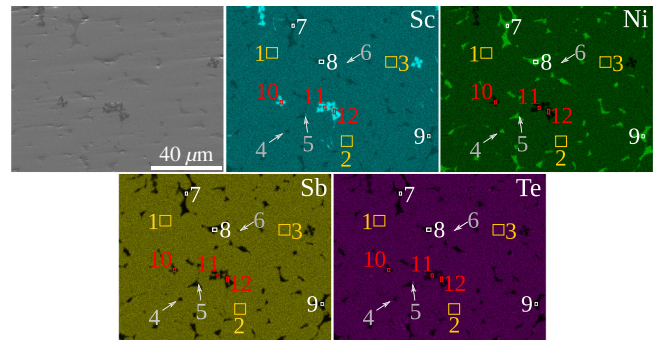


FIG. 2. SEM image and EDS elemental mapping for  $\text{ScNiSb}_{0.85}\text{Te}_{0.15}$ . The scale bar applies for all panels. The reader is referred to Table II for quantitative analyses of the marked areas.

other half-Heusler compounds based on RE elements in order to evaluate possibilities of  $n$ -type doping by intrinsic and extrinsic defect formation. For all the specimens, we find tiny amounts of impurities: either elemental nickel or NiSb. The summed content of contaminants in any sample does not exceed 4 vol.%. The experimental density is close to the theoretical one, see  $d_{\text{exp}}$  for the absolute and  $d_{\text{rel}}$  for the relative values in Table SII within the Supplemental Material [50].

The SEM imaging and chemical EDS mapping obtained for the  $\text{ScNiSb}_{0.85}\text{Te}_{0.15}$  sample is shown in Fig. 2 and quantified in Table II. The SEM image proves that the sample is free from crack and gas voids. The average composition of the main phase denoted by areas 1–3 in EDS panels of Fig. 2 is  $\text{Sc}_{33.2(1)}\text{Ni}_{32.5(2)}\text{Sb}_{30.2(2)}\text{Te}_{4.0(0)}$ ,

TABLE II. Results of the EDS analysis for  $\text{ScNiSb}_{0.85}\text{Te}_{0.15}$ . The listed areas correspond to those marked in Fig. 2.

Area	Sc (at.%)	Ni (at.%)	Sb (at.%)	Te (at.%)
1	33.1	32.4	30.5	4.0
2	33.2	32.7	30.1	4.0
3	33.3	32.5	30.2	4.0
Average	$\text{Sc}_{33.2(1)}\text{Ni}_{32.5(2)}\text{Sb}_{30.2(2)}\text{Te}_{4.0(0)}$			
4	31.5	16.7	23.5	28.3
5	33.7	24.8	9.9	31.6
6	37.2	25.7	13.0	24.1
Average	$\text{Sc}_{34(3)}\text{Ni}_{22(5)}\text{Sb}_{16(7)}\text{Te}_{28(4)}$			
7	22.9	73.5	2.2	1.4
8	23.2	70.5	4.6	1.7
9	21.6	75.2	1.8	1.3
Average	$\text{Sc}_{23(1)}\text{Ni}_{73(2)}\text{Sb}_{3(2)}\text{Te}_{1.5(2)}$			
10	85.3	6.0	6.7	2.0
11	82.0	8.2	7.1	2.7
12	86.8	5.2	5.9	2.0
Average	$\text{Sc}_{85(2)}\text{Ni}_{7(2)}\text{Sb}_{7(1)}\text{Te}_{2.2(4)}$			

which corresponds to  $\text{Sc}_{97.1(3)}\text{Ni}_{95.0(6)}\text{Sb}_{88.3(6)}\text{Te}_{11.7(1)}$  if normalized to the most occupied  $4b$  atomic site ( $\text{Sb}+\text{Te}$ ). Slight deficiency in Sc and Ni is in agreement with the findings from XRD analysis. The actual content of tellurium is somewhat smaller with respect to the nominal composition, which is likely due to the high volatility of this element and formation of minuscule Te-rich precipitations (numbers 4–6 in Fig. 2). Points 7–9 denote elemental nickel or solid solution  $\text{Ni}_{1-x}\text{Sc}_x$  with dominant Ni content, uncovered also by the Rietveld refinement. Rectangles 10–12 are scandium-rich regions, which might correspond to either metallic Sc, or  $\text{Sc}_2\text{O}_3$  in a quantity too small to be detected by XRD. Similar results are obtained for all the other  $\text{ScNiSb}_{1-x}\text{Te}_x$  samples, see Figs. S2, S3 and Table SI within the Supplemental Material [50].

Figure 3(a) displays the temperature dependencies of the carrier concentration obtained from the Hall-effect measurements. Positive sign of  $n$  for the pristine  $\text{ScNiSb}$  sample implies that holes constitute the majority charge carriers. The temperature dependence of  $n$  in this specimen is rather complex, which most likely results from multivalley effects, similarly to other  $p$ -type HH phases [19,54]. The carrier concentration for the doped  $\text{ScNiSb}_{1-x}\text{Te}_x$  materials, calculated directly from the Hall voltage turns to negative sign, which proves successful electron doping. In the  $\text{ScNiSb}_{1-x}\text{Te}_x$  samples with  $x = 3, 5, 10\%$ , the temperature dependence of the carrier concentration is rather weak, indicative of a degenerate conductivity regime. For  $\text{ScNiSb}_{0.85}\text{Te}_{0.15}$  in turn, the temperature dependence of  $|n|$  is similar to that of pristine  $\text{ScNiSb}$ . Likely, the chemical potential in this specimen is deep enough in the conduction band for multivalley effects to occur. Above 100 K though, the carrier concentration is weakly dependent on temperature for all the specimens investigated. At 300 K, the absolute values of  $n$  increase with rising Te content, see Fig. S5 within the Supplemental Material [50]. The increase in  $n$  with dopant content is monotonic; deviations from perfect linear behavior in  $n(x)$  might be ascribed to experimental error of Hall measurement, crystallographic disorder, and complex microstructure of the

studied specimens. Even an amount of metallic Ni or  $\text{NiSb}$  as small as 4 vol.% might contribute additional carriers to the semiconducting half-Heusler matrix.

The temperature dependencies of the Hall mobility are plotted in Fig. 3(b). The mobility increases with rising temperature, which might result from mixed scattering of charge carriers on ionized impurities ( $\mu_H \propto T^{3/2}$ ) [55] and grain boundaries ( $\mu_H \propto \exp[-1/T]$ ) [56]. Finding of similar behavior in mobility single-crystal  $\text{ZrNiSn}$  [57] (free from grain-boundary influence) indicates that the former mechanism is more likely to be dominant in pristine  $\text{ScNiSb}$ . Such scattering is not desired for TE materials, as it usually results in small values of  $\mu_H$  [56,58]. With Te doping, the increase in  $\mu_H$  with temperature is gradually suppressed, however, the values of  $\mu_H$  rise substantially. Such behavior can be ascribed to a change of the dominant scattering mechanism to either point defect ( $\mu_H \propto T^{-1/2}$ ) [59] or acoustic phonon ( $\mu_H \propto T^{-3/2}$ ) [55] scattering, which are commonly observed for state-of-the-art thermoelectrics [55,56,58,59]. Recent studies showed that increasing carrier concentration in  $\text{ZrNiSn}$  can lead to a change of the dominant scattering mechanism from ionized impurity to acoustic phonon scattering [57]. The effect is explained by increased screening of ionized impurity centers by dense electron gas in the degenerate regime. We suggest that a similar phenomenon might be a driving force for the change of scattering mechanism with doping in  $\text{ScNiSb}$ . Quantitative analysis of scattering mechanisms in  $\text{ScNiSb}$  appear to be an exciting topic for further studies.

Nonmonotoneous variation of  $\mu_H$  at room temperature with increasing Te content is probably due to synthesis-dependent changes of microstructure. These variations though, do not affect the general picture of mobility rising roughly by an order of magnitude due to electron doping from about  $0.7 \text{ cm}^2\text{V}^{-1}\text{s}^{-1}$  in  $p$ -type  $\text{ScNiSb}$  to  $6 - 17 \text{ cm}^2\text{V}^{-1}\text{s}^{-1}$  for the  $n$ -type specimens. Here, it is worthwhile to recall that the previous analysis of bipolar thermal conductivity in  $\text{ScNiSb}$  predicted enhancement of the charge mobility in this compound due to  $n$ -type doping by a factor of 8 [19], which is satisfactory agreement

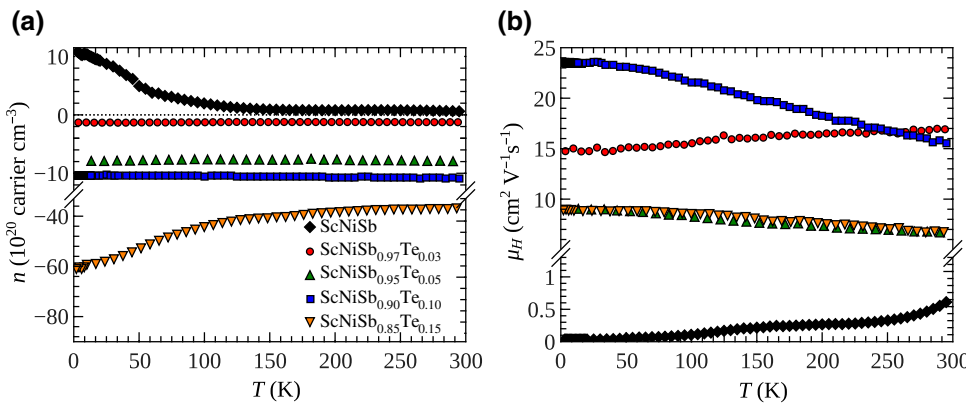


FIG. 3. Low-temperature (2–300 K) Hall-effect data for  $\text{ScNiSb}_{1-x}\text{Te}_x$ : (a) carrier concentration, (b) Hall mobility.

with the experimental result, bearing in mind all the simplifications of the model applied. Interestingly, the absolute values of mobility in our undoped sample are still smaller than that of prototype thermoelectric half-Heusler ZrNiSn ( $\mu_H > 20 \text{ cm}^2 \text{V}^{-1} \text{s}^{-1}$  at  $T > 100 \text{ K}$ ) [1]. In turn, similar  $\mu_H$  is observed for the ScNiSb specimen obtained with spark plasma sintering [19], which suggests that SPS technique should be used in further thermoelectric studies of ScNiSb.

The high-temperature electrical resistivity of the  $\text{ScNiSb}_{1-x}\text{Te}_x$  samples is shown in Fig. 4(a). For ScNiSb, it decreases in a manner typical for intrinsic semiconductors. The data above 500 K is analyzed with the Arrhenius formula describing thermal activation of charge carriers

$$1/\rho = \sigma_0 \exp(-E_g/2k_B T), \quad (1)$$

where  $E_g$  denotes the band gap and  $\sigma_0$  corresponds to the conductivity coefficient. The parameters obtained via least-squares fitting are  $E_g = 404(2) \text{ meV}$ ,  $\sigma_0 = 0.44(1) \mu\Omega^{-1} \text{m}^{-1}$ . The value of  $E_g$  is in the upper range of the band gaps reported for ScNiSb in the literature [16,18–22]. With increasing tellurium content,  $\rho(T)$  gradually changes towards behavior typical for degenerate semiconductors, in concert with results of carrier-concentration measurement. The resistivity decreases substantially with Te doping due to simultaneous increase of the carrier concentration and the mobility (see above). The absolute value of resistivity is higher than in previous literature works most likely due to lower  $\mu_H$  in the current study (see above) [16,18,21,22].

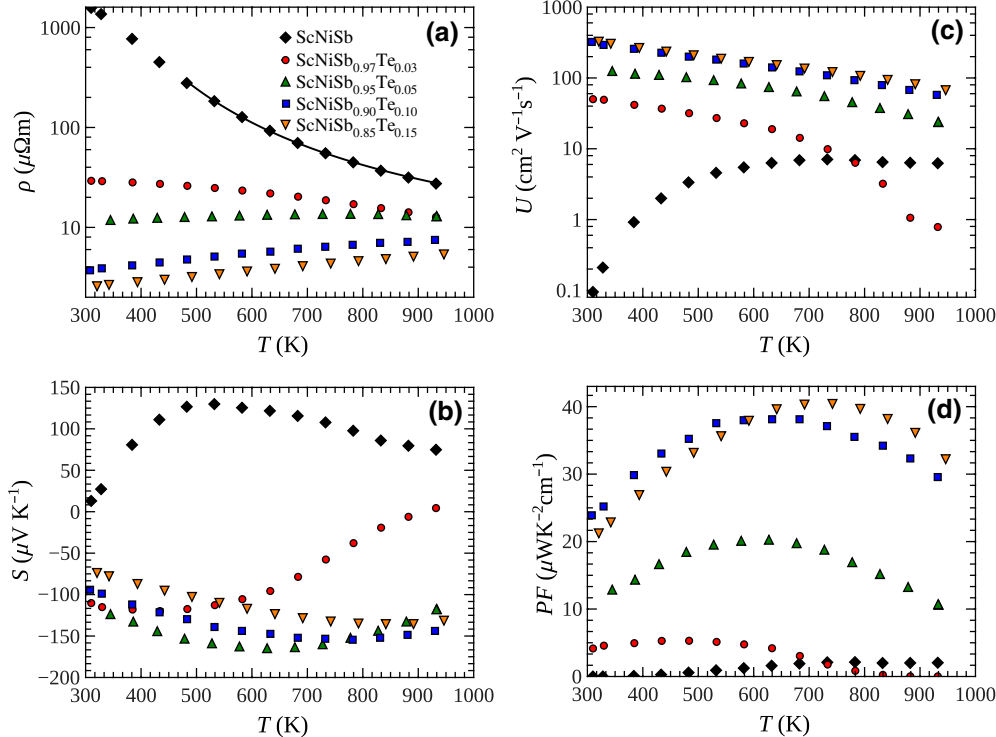


Figure 4(b) shows the temperature dependencies of the Seebeck coefficient for the  $\text{ScNiSb}_{1-x}\text{Te}_x$  series. Consistently with the Hall data, thermopower switches its sign from positive for pristine ScNiSb to negative for the Te-doped specimens. Maximum in  $S$  corresponding to minority carrier activation is pushed towards higher temperatures with doping, from 530 K for ScNiSb to 890 K for  $\text{ScNiSb}_{0.85}\text{Te}_{0.15}$ . Fast activation of minority carriers in  $p$ -type specimens results most likely from superior mobility of electrons [60]. Absolute values of the thermopower at room temperature decrease with rising Te content due to increasing carrier concentration. The so-called Seebeck gap ( $E_g^*$ ) is calculated from the Goldsmid-Sharp formula [61], relating the value of the Seebeck coefficient at its maximum ( $S_{\max}$ ) to its position on the temperature scale ( $T_{\max}$ ):

$$S_{\max} = E_g^*/2eT_{\max}. \quad (2)$$

For the values of  $E_g^*$  in  $\text{ScNiSb}_{1-x}\text{Te}_x$  the reader is referred to Table III. In  $p$ -type ScNiSb, the Seebeck gap is strongly reduced with respect to the value of the band gap obtained from the resistivity analysis ( $E_g$ ). This effect probably results from high weighted mobility ratio in favor of minority charge carriers and small  $E_g$  in ScNiSb, causing violation of Maxwell-Boltzmann statistics [61,62]. Quantitative analysis of the weighted mobility ratio based on differences between  $E_g^*$  and the real band gap can provide valuable information on TE performance [60,62]. Its applicability, however, is limited to materials with a Seebeck

FIG. 4. High-temperature thermoelectric properties of  $\text{ScNiSb}_{1-x}\text{Te}_x$ : (a) electrical resistivity, (b) Seebeck coefficient, (c) weighted mobility, (d) power factor. Note the logarithmic y-axis scale in (a),(c). Solid line in (a) represents the Arrhenius fit [Eq. (1)].

TABLE III. Parameters characterizing electronic transport in  $\text{ScNiSb}_{1-x}\text{Te}_x$ : Seebeck band gap  $E_g^*$  [Eq. (2)], room-temperature effective mass  $m_{\text{eff}}$  [Eq. (5)], Hall mobility  $\mu_H$ , intrinsic mobility  $\mu_0$  [Eq. (7)], weighted mobility  $U$  [Eq. (9)], effective mass from validation of weighted mobility  $m_{\text{eff-}U}$  [Eq. (11)], and maximum power factor  $PF_{\text{max}}$ .

	$E_g^*$ (meV)	$m_{\text{eff}} (m_e)$	$\mu_H (\text{cm}^2 \text{V}^{-1} \text{s}^{-1})$	$\mu_0 (\text{cm}^2 \text{V}^{-1} \text{s}^{-1})$	$U (\text{cm}^2 \text{V}^{-1} \text{s}^{-1})$	$m_{\text{eff-}U} (m_e)$	$PF_{\text{max}} (\mu \text{WK}^{-2} \text{cm}^{-1})$
ScNiSb	138(4)	0.10(8)	0.68(2)	3.2(3)	0.095(8)	0.10(8)	2.3(3)
$\text{ScNiSb}_{0.97}\text{Te}_{0.03}$	106(3)	1.5(1)	16.7(5)	28(2)	50(4)	1.5(1)	5.3(7)
$\text{ScNiSb}_{0.95}\text{Te}_{0.05}$	206(6)	5.2(4)	6.6(2)	10.4(8)	123(10)	5.2(4)	20(3)
$\text{ScNiSb}_{0.90}\text{Te}_{0.10}$	246(7)	5.1(4)	15.1(5)	28(2)	321(26)	5.1(4)	38(5)
$\text{ScNiSb}_{0.85}\text{Te}_{0.15}$	242(7)	8.4(7)	6.3(2)	13(1)	325(26)	8.7(7)	40(5)

coefficient well above  $150 \mu\text{V/K}$  [62], which is why we refrain from using this model for  $\text{ScNiSb}_{1-x}\text{Te}_x$  series.

For the Te-doped specimens, which are no longer affected by small mobility of their majority carriers, the values of  $E_g^*$  rise according to expectations. Even for the specimens with the largest doping, however,  $E_g^*$  does not reach the magnitude of  $E_g$ , which signals difficulties in application of Eq. (2) to materials with a relatively small Seebeck coefficient ( $S < 150 \mu\text{V/K}$ ) [62]. Literature values of Seebeck coefficient for ScNiSb at 300 K span in a wide range from  $65 \mu\text{V K}^{-1}$  [22] through  $120 \mu\text{V K}^{-1}$  at 300 K and similar maximum of c.a.  $150 \mu\text{V K}^{-1}$  in Refs. [16,21], up to  $200 \mu\text{V K}^{-1}$  at 300 K for the SPS-prepared sample [18]. Such a wide range of attainable thermopowers depending on the synthesis conditions is typical for half-Heusler phases based on RE elements most likely due to strong dependence of their transport properties on disorder [16].

With the help of the parabolic band model (PBM) [63], one can calculate the dependence of a Seebeck coefficient on the chemical potential ( $\eta$ )

$$S = \frac{k_B}{e} \left[ \frac{2F_1(\eta)}{F_0} - \eta \right], \quad (3)$$

where  $F_j(\eta)$  denotes the Fermi integral of order  $j$

$$F_j(\eta) = \int_0^\infty \frac{\zeta^j (d\zeta)}{1 + \exp(\zeta - \eta)}. \quad (4)$$

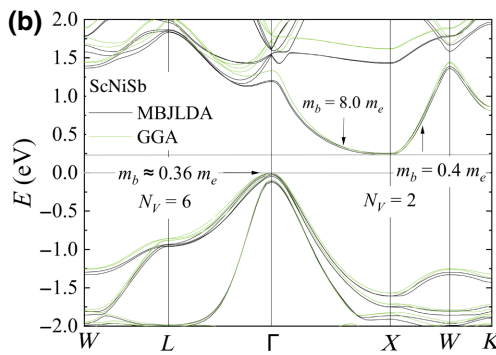
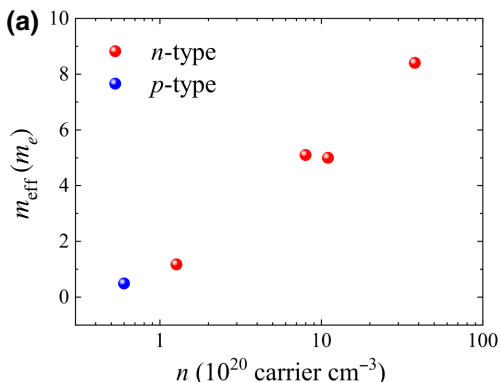


FIG. 5. (a) Dependence of effective mass in  $\text{ScNiSb}_{1-x}\text{Te}_x$  series on carrier concentration and (b) band structure of ScNiSb with data from Ref. [20].

the effective masses are derived also at 380 K, and collected in Table SII [50]. The  $m_{\text{eff}}$  value found for ScNiSb is much closer to literature data. At the same time, the values obtained for the Te-doped samples are nearly the same as those measured at room temperature. Some remaining difference between  $m_{\text{eff}}$  derived *ab initio* and the experimental results are likely due to synthesis-sensitive disorder in the crystal structure of ScNiSb, affecting strongly the electronic properties of the material.

Within the series  $\text{ScNiSb}_{1-x}\text{Te}_x$  the effective masses rise significantly for the doped specimens, see Fig. 5(a). Such an effect is anticipated based on the band structure of ScNiSb [20]. The conduction band in this compound is highly anisotropic: the band masses are equal to  $8.0m_e$  in  $\Gamma$ - $X$  direction and  $0.4m_e$  for  $\Gamma$ - $W$  direction, see Fig. 5(b). Taking into account twofold degeneracy of the conduction band in ScNiSb, the *ab initio* *n*-type effective masses are equal to  $12.7m_e$  and  $0.65m_e$  in those directions, respectively.

The ratio of  $m_{\text{eff}}$  in two directions (the anisotropy factor, AF) is equal to 19.5. Recently, good *n*-type TE performance of classical HH compound ZrNiSn is explained as originating from a high AF of 6 for its conduction band [64]. Anisotropic band is expected to support the material with both heavy carriers essential for large thermopower, as well as some portion of light carriers providing good electrical conductivity. Large values of AF for ScNiSb are very promising for further optimization of its TE properties.

As a next step of the electron transport analysis in the  $\text{ScNiSb}_{1-x}\text{Te}_x$  series, we estimate the upper limit of charge-carrier mobility ( $\mu_0$ ) in the fully intrinsic regime using the formula [65]

$$\mu_H = \mu_0 \frac{F_{-1/2}}{2F_0}. \quad (7)$$

The value of  $\mu_0$  allows calculations of the weighted mobility ( $U$ ), defined by Slack [66] as

$$U = \mu_0 \left( \frac{m_{\text{eff}}}{m_e} \right)^{3/2}. \quad (8)$$

This coefficient serves as a guide in comparing TE materials, as maximum performance available by tuning carrier concentration is proportional to  $U$ , and  $U$  is connected to the TE quality factor ( $B$ ) as  $B = (8k_B/3e)^2 [8e\pi^2(2m_e k_B T)^{3/2}/3h^3](U/\kappa_L)T$ , where  $\kappa_L$  corresponds to the lattice thermal conductivity [66]. For  $\text{ScNiSb}_{1-x}\text{Te}_x$ , the simultaneous increase in  $\mu_0$  and  $m_{\text{eff}}$  with tellurium doping yields considerable enhancement in the TE properties.

At high temperatures, where Hall data are not available, the weighted mobility of the majority carriers can be estimated applying the approximation in the Drude-Sommerfeld free-electron model [67]:

$$U = \frac{3h^3}{8\pi e(2m_e k_B T)^{3/2}} \times \frac{1}{\rho} \left( \frac{\exp\left(\frac{|S|}{k_B/e} - 2\right)}{1 + \exp\left[-5\left(\frac{|S|}{k_B/e} - 1\right)\right]} + \frac{\frac{3}{\pi^2} \frac{|S|}{k_B/e}}{1 + \exp\left[5\left(\frac{|S|}{k_B/e} - 1\right)\right]} \right). \quad (9)$$

After reducing constants, one can rewrite this formula in a simpler form:

$$U = 3310 \left[ \frac{\text{cm}^2}{\text{Vs}} \right] \left( \frac{1}{\rho [\mu\Omega\text{m}]} \right) \left( \frac{T [\text{K}]}{300} \right)^{-3/2} \left( \frac{\exp\left(\frac{|S|}{k_B/e} - 2\right)}{1 + \exp\left[-5\left(\frac{|S|}{k_B/e} - 1\right)\right]} + \frac{\frac{3}{\pi^2} \frac{|S|}{k_B/e}}{1 + \exp\left[5\left(\frac{|S|}{k_B/e} - 1\right)\right]} \right). \quad (10)$$

The approximation is correct within 3% for Seebeck coefficient values, when  $|S| > 20 \mu\text{VK}^{-1}$  [67]. The temperature dependencies of  $U$  obtained for the  $\text{ScNiSb}_{1-x}\text{Te}_x$  series from Eq. (10) are shown in Fig. 4(c). In our previous work [19] we predicted that  $U$  in ScNiSb should considerably rise with *n*-type doping. Asymmetry between the valence and conduction band is also shown to be beneficial for TE properties in the general case using *ab initio* calculations [68]. In  $\text{ScNiSb}_{1-x}\text{Te}_x$  the enhancement in  $U$  with *n*-type doping is indeed very strong, see Fig. S5 within

the Supplemental Material [50]. The weighted mobility in  $\text{ScNiSb}_{0.85}\text{Te}_{0.15}$  reaches  $325 \text{ cm}^2\text{V}^{-1}\text{s}^{-1}$  at room temperature. Similar or lower values of  $U$  near 300 K are reported before for the state-of-the-art thermoelectrics:  $\text{Na}_x\text{Co}_3\text{Sb}_{12}$  skutterudites ( $U = 340 \text{ cm}^2\text{V}^{-1}\text{s}^{-1}$ ) [69], FeNbSb-based HH thermoelectric ( $U = 330 \text{ cm}^2\text{V}^{-1}\text{s}^{-1}$ ) [15],  $\text{Bi}_2\text{Te}_3$  ( $U = 250 \text{ cm}^2\text{V}^{-1}\text{s}^{-1}$ ) [70], or *p*-type PbTe ( $U = 130 \text{ cm}^2\text{V}^{-1}\text{s}^{-1}\text{K}$ ) [71].

A large magnitude of the weighted mobility ratio in favor of electrons is previously reported also for

ZrNiSn [53,60]. In the latter case, the Ni partial occupancy at the nominally empty Wyckoff site  $4d(3/4, 3/4, 3/4)$  leads to the formation of in-gap states nearby the conduction-band minimum. This feature causes a decrease in effective band gap with respect to the value obtained from *ab initio* calculations for a disorder-free compound. Furthermore, holes originating from the impurity band are expected to bear strongly enhanced effective mass, and thus relatively low mobility. Despite some similarities, the case of ZrNiSn cannot be treated as a direct analog to the current study. The undoped samples of ScNiSb are always *p*-type [16,18,21,22], while pristine ZrNiSn specimens are *n*-type [60], which suggests different native defects for the two compounds. Furthermore, for ScNiSb we do not observe strongly reduced band gap with respect to the *ab initio* results (see above). Most importantly, Ni interstitials are not reported in high-quality diffraction studies on ScNiSb [18]. Instead, Ni split positions are detected [18]. Also in the current study with laboratory XRD we did not detect a sizable amount of Ni interstitials (see above). Influence of Ni split positions on the band structure of ScNiSb and possibly other RE-bearing HH phases appears to be a fascinating topic for further *ab initio* studies.

In order to ensure that the approximation of  $U$  based only on the resistivity and thermopower data, is correct, we calculate the weighted mobility effective masses ( $m_{\text{eff}}^U$ ) from the formula

$$U = \mu_0 \left( \frac{m_{\text{eff}}^U}{m_e} \right)^{3/2}. \quad (11)$$

The results are gathered in Table III (room temperature) and in Table SII within the Supplemental Material ( $T = 380$  K) [50]. The observed excellent agreement at room temperature and 380 K between  $m_{\text{eff}}$  and  $m_{\text{eff}}^U$  proves the correctness of the approach given by Eq. (10) in the calculations performed.

The thermoelectric power factor ( $PF = S^2/\rho$ ) derived for the  $\text{ScNiSb}_{1-x}\text{Te}_x$  series is shown in Fig. 4(d). Clearly, the magnitude of the  $PF$  is substantially enhanced due to the tellurium doping. Figure S5 within the Supplemental Material [50] shows that an increase in  $PF$  is precisely correlated with rising weighted mobility as a function of Te content. The maximum of  $40 \mu\text{WK}^{-2} \text{cm}^{-1}$  is obtained at 740 K for  $\text{ScNiSb}_{0.85}\text{Te}_{0.15}$ . Comparable results are reported for the state-of-the-art thermoelectric materials, e.g.,  $\text{Bi}_2\text{Te}_3$  ( $PF_{\text{max}} = 38 \mu\text{WK}^{-2} \text{cm}^{-1}$ ) [70], PbTe-based thermoelectrics ( $PF_{\text{max}} = 33 \mu\text{WK}^{-2} \text{cm}^{-1}$ ) [71], and  $\text{Fe}_x\text{Co}_3\text{Sb}_{12}$  skutterudites ( $PF_{\text{max}} = 36 \mu\text{WK}^{-2} \text{cm}^{-1}$ ) [72]. It is worthwhile to recall that the magnitude of  $PF$  is recently shown to be a more relevant indicator for the performance of TE material than the figure of merit ( $ZT$ ) [73,74]. Contemporary applications, e.g., powering space missions, require

high efficiency of energy conversion (high  $ZT$ ) due to limited heat supply. In turn, for the prospect functionalities of thermoelectrics, which is waste-heat recovery from large energy sources like power plants or ironworks and glass-works, it is more useful to achieve large electrical power density (high  $PF$ ), and tailored but not minimal thermal conductivity, as the vast majority of heat-emitting devices require dynamic cooling [73].

Bearing in mind that the current paper showcases the successful *n*-type doping of ScNiSb, a large space for optimization is foreseen for this compound. The most promising directions appear to be (i) synthesis-technique development leading to more phase-pure samples with even higher charge-carrier mobility, and (ii) doping towards even larger *n*-type carrier concentration in order to push the bipolar effects to higher temperatures and further reduce the electrical resistivity. We evaluate possibilities of further improvement in thermoelectric properties with PBM formalism for the sample with the highest  $PF$ ,  $\text{ScNiSb}_{0.85}\text{Te}_{0.15}$ . At each value of carrier concentration from the range  $1 \times 10^{18} \text{ cm}^{-3}$  to  $1 \times 10^{23} \text{ cm}^{-3}$  we solve Eq. (5) for chemical potential and use the so-obtained value of  $\eta$  for calculating the Seebeck coefficient from Eq. (3), intrinsic mobility from Eq. (7), and the Lorenz number using formula [75]

$$L = \left( \frac{k_B}{e} \right)^2 \times \frac{3F_0F_2 - 4F_1^2}{F_0^2}. \quad (12)$$

Next, we calculate the material-independent parameter  $\psi$  [75]:

$$\psi = \frac{8\pi e}{3} \left( \frac{2m_e k_B}{h^2} \right)^{3/2} F_0, \quad (13)$$

and the quality factor  $\beta$  [75]:

$$\beta = \frac{\mu_0 (m_{\text{eff}}/m_e)^{3/2} T^{5/2}}{\kappa_L}. \quad (14)$$

Finally, we calculate the following equation for the prediction of  $ZT$  values [75]:

$$ZT = \frac{S^2}{L + (\psi\beta)^{-1}}. \quad (15)$$

We assume that the effective mass obtained from Hall measurement does not vary with temperature. Lattice thermal conductivity at each temperature is adapted from Ref. [19]. A roughly similar  $L$  value obtained at high temperatures for ScNiSb synthesized by arc melting combined with spark plasma sintering [19] and arc melting alone [16] support the reliability of this approach. Incorporation of tellurium in  $\text{ScNiSb}_{0.85}\text{Te}_{0.15}$  might reduce  $\kappa_L$  with respect to values obtained for pure ScNiSb, so it is helpful to keep in mind,

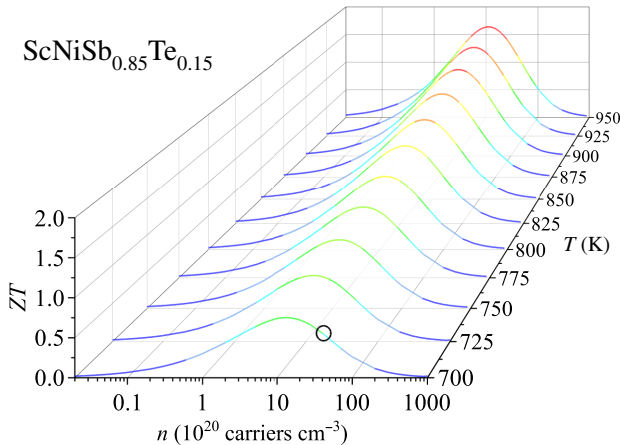


FIG. 6. Single parabolic band-model predictions for thermoelectric performance of  $\text{ScNiSb}_{0.85}\text{Te}_{0.15}$ . The black open circle marks estimate experimental  $ZT$  obtained with thermal conductivity from Ref. [16].

that the predicted  $ZT$  might be slightly underestimated with respect to reality.

The results are shown in Fig. 6. With rising temperature, the maximum of predicted  $ZT$  increase, reaching maximum of 1.63 at 950 K. Here, it is necessary to mention, that this kind of modeling is relevant for materials with single dominant carrier type. In other words, to benefit from increased  $ZT$  in  $\text{ScNiSb}_{0.85}\text{Te}_{0.15}$ , it is necessary to push activation of minority charge carriers to above 950 K. This can be achieved, e.g., by synthesized solid solution  $\text{ScNi}_{1-y}\text{Pt}_y\text{Sb}_{1-x}\text{Te}_x$ , as  $\text{ScPtSb}$  is characterized by a significantly bigger *ab initio* energy gap  $E_g = 0.42$  meV with generalized gradient approximation (GGA) potential and 0.63 with modified Becke-Johnson local density approximation (MBJLDA), while  $\text{ScNiSb}$  exhibits *ab initio*  $E_g = 0.24$  eV regardless of the potential used [20]. In order to make the discussion on band-gap values more transparent, we prepare the band-structure plot for  $\text{ScPtSb}$  (Fig. S6) and mark the band gap with gray lines. Also for the plot of band structure for  $\text{ScNiSb}$  [Fig. 5(b)] the band gap is marked with gray lines.

Increasing the energy gap of  $\text{ScNi}_{1-y}\text{Pt}_y\text{Sb}_{1-x}\text{Te}_x$  will likely decrease the amount of charge carriers, which is in line with demands of PBM. The experimental carrier concentration of  $\text{ScNiSb}_{0.85}\text{Te}_{0.15}$  is  $4 \times 10^{21} \text{ cm}^{-3}$ , while maximum performance is predicted at  $1 \times 10^{21} \text{ cm}^{-3}$  (see Fig. 6). The estimate experimental figure of merit for  $\text{ScNiSb}_{0.85}\text{Te}_{0.15}$  using thermal conductivity from Ref. [19] is shown by the black circle on the curve obtained with  $T = 700$  K.

Similarly to  $\text{ScNiSb}$ ,  $\text{ScPtSb}$  possess a heavy branch of the conduction band in  $X-\Gamma$  direction and a light branch at  $X-W$  direction (see Fig. S6 within the Supplemental Material [50]). *Ab initio* calculations performed for  $\text{ScPtSb}$  with GGA potential, suggest that additional

conduction band with minimum at  $\Gamma$  point might contribute to electron transport [20], see Fig. S6 within the Supplemental Material [50]. Interestingly, the band structure of  $\text{ScPtSb}$  obtained with the MBJLDA potential do not have this feature, the conduction band at  $\Gamma$  point in this case is located at higher energies than the anisotropic band from  $X$  point. This complex situation makes the study of  $\text{ScNi}_{1-y}\text{Pt}_y\text{Sb}_{1-x}\text{Te}_x$  solid solutions even more exciting.

For further research, we also suggest applying electron doping in other representatives of RE-bearing HH phases due to the similarity of their electron in band structures [20, 76, 77], see, e.g.,  $\text{ScNiSb}$ ,  $\text{ScPdSb}$ ,  $\text{YNiSb}$ ,  $\text{TmNiSb}$ ,  $\text{ErNiSb}$ ,  $\text{LuNiSb}$ . In our initial experimental analysis of the bipolar thermal conductivity we establish that the  $\text{RENiSb}$  compounds with  $\text{RE} = \text{Dy}, \text{Er}, \text{Tm}, \text{Lu}$ , are characterized by even higher mobility ratio in favor of electrons than  $\text{ScNiSb}$ , up to 31.5 for  $\text{TmNiSb}$  [19]. Furthermore, it is found that those materials exhibit significantly smaller lattice thermal conductivity in pristine form than their *d*-electron counterparts. This feature is driven by their lower Debye temperature and intense point-defect scattering due to intrinsic structural disorder [19]. We speculate, that RE-bearing HH phases might turn out to be an alternative family of excellent thermoelectrics due to the combination of superior *n*-type electron transport and naturally small thermal conductivity.

#### IV. CONCLUSIONS

We aim to verify the outcome of bipolar-thermal-conductivity analysis for half-Heusler compound  $\text{ScNiSb}$ , which suggests high mobility of charge carriers if synthesized as a *n*-type material [19]. In order to prove the presumption, series of  $\text{ScNiSb}_{1-x}\text{Te}_x$  specimens with  $x = 0, 0.03, 0.05, 0.10, 0.15$  is prepared by arc melting and annealing. The x-ray diffraction and the EDS analysis show consistently that the HH matrix in the obtained materials is slightly deficient in Ni and Sc. From the perspective of electron transport, relatively small tellurium content in  $\text{ScNiSb}_{1-x}\text{Te}_x$  samples is enough to tune the system towards *n*-type behavior. In line with the prediction, electrons in  $\text{ScNiSb}$  turn out to be roughly an order of magnitude more mobile than holes. The dominant scattering mechanisms changed most likely from ionized impurity interaction to mixture of acoustic phonon and alloy influence. We also observe a considerable increase in the effective mass of charge carriers, which is consistent with *ab initio* band-structure calculations. These two effects lead to considerable enhancement in weighted mobility, up to  $325 \text{ cm}^2\text{V}^{-1}\text{s}^{-1}$  at 300 K for  $\text{ScNiSb}_{0.85}\text{Te}_{0.15}$ . Large  $U$  resulted in a superior thermoelectric power factor of  $40 \mu\text{WK}^{-2} \text{ cm}^{-1}$  at 740 K for the same compound. Our finding shows that  $\text{ScNiSb}$  might be a gateway to an alternative family of excellent TE materials, namely RE-bearing HH phases. Based on our previous analysis

of mobility ratio, a few representatives of the group are expected to even exceed ScNiSb in their advantageous electron properties [19]. Furthermore, they also exhibit small lattice thermal conductivity due to low Debye temperature and intrinsic disorder leading to strong scattering of phonons. As a result, we anticipate excellent TE performance for these compounds.

## ACKNOWLEDGMENTS

The authors thank Professor G. Jeffrey Snyder for valuable discussions and comments on the data included in the current paper. This work is supported by the National Science Centre (Poland) under research Grant No. 2015/18/A/ST3/00057.

- 
- [1] F. Aliev, Gap at Fermi level in some new d- and f-electron intermetallic compounds, *Physica B* **171**, 199 (1991).
- [2] Y. V. Stadnyk, L. Romaka, A. Goryn, Y. K. Gorelenko, J. Pierre, and R. Skolozdra, Solid solutions  $ZrNi_{1-x}M_xSn$  ( $M = Cr, Mn, Cu$ ) and their electrical and magnetic properties, *J. Alloys Compd.* **262**, 476 (1997).
- [3] H. Hohl, A. P. Ramirez, C. Goldmann, G. Ernst, B. Wölfling, and E. Bucher, Efficient dopants for ZrNiSn-based thermoelectric materials, *J. Phys.: Condens. Matter* **11**, 1697 (1999).
- [4] C. Uher, J. Yang, S. Hu, D. Morelli, and G. Meisner, Transport properties of pure and doped MNiSn ( $M = Zr, Hf$ ), *Phys. Rev. B* **59**, 8615 (1999).
- [5] K. Mastronardi, D. Young, C.-C. Wang, P. Khalifah, R. J. Cava, and A. Ramirez, Antimonides with the half-Heusler structure: New thermoelectric materials, *Appl. Phys. Lett.* **74**, 1415 (1999).
- [6] T. Zhu, C. Fu, H. Xie, Y. Liu, and X. Zhao, High efficiency half-Heusler thermoelectric materials for energy harvesting, *Adv. Energy Mater.* **5**, 1500588 (2015).
- [7] F. Aliev, J. Calleja, N. Mestres, R. Villar, S. Vieira, V. Pryadun, A. Leventsov, and R. Scolozdra, Localization induced transformation of the lattice modes of MNiSn ( $M = Zr, Hf, Ti$ ) compounds, *Physica B* **194**, 1089 (1994).
- [8] G. Rogl, A. Grytsiv, M. Gürth, A. Tavassoli, C. Ebner, A. Wünschek, S. Puchegger, V. Soprunya, W. Schranz, E. Bauer, H. Müller, M. Zehetbauer, and P. Rogl, Mechanical properties of half-Heusler alloys, *Acta Mater.* **107**, 178 (2016).
- [9] E. Rausch, B. Balke, S. Ouardi, and C. Felser, Long-term stability of (Ti/Zr/Hf)CoSb<sub>1-x</sub>Sn<sub>x</sub> thermoelectric p-type half-Heusler compounds upon thermal cycling, *Energy Tech.* **3**, 1217 (2015).
- [10] G. Joshi, R. He, M. Engber, G. Samsonidze, T. Pantha, E. Dahal, K. Dahal, J. Yang, Y. Lan, B. Kozinsky, and Z. Ren, NbFeSb-based p-type half-Heuslers for power generation applications, *Energy Environ. Sci.* **7**, 4070 (2014).
- [11] C. Yu, T.-J. Zhu, R.-Z. Shi, Y. Zhang, X.-B. Zhao, and J. He, High-performance half-Heusler thermoelectric materials  $Hf_{1-x}Zr_xNiSn_{1-y}Sb_y$  prepared by levitation melting and spark plasma sintering, *Acta Mater.* **57**, 2757 (2009).
- [12] M. Gürth, G. Rogl, V. Romaka, A. Grytsiv, E. Bauer, and P. Rogl, Thermoelectric high ZT half-Heusler alloys  $Ti_{1-xy}Zr_xHf_yNiSn$  ( $0 \leq x \leq 1; 0 \leq y \leq 1$ ), *Acta Mater.* **104**, 210 (2016).
- [13] H. Zhu, J. Mao, Y. Li, J. Sun, Y. Wang, Q. Zhu, G. Li, Q. Song, J. Zhou, Y. Fu, R. He, T. Tong, Z. Liu, W. Ren, L. You, Z. Wang, J. Luo, A. Sotnikov, J. Bao, K. Nielsch, G. Chen, D. J. Singh, and Z. Ren, Discovery of TaFeSb-based half-Heuslers with high thermoelectric performance, *Nat. Commun.* **10**, 270 (2019).
- [14] H. Zhu, R. He, J. Mao, Q. Zhu, C. Li, J. Sun, W. Ren, Y. Wang, Z. Liu, Z. Tang, A. Sotnikov, Z. Wang, D. Broido, D. J. Singh, G. Chen, K. Nielsch, and Z. Ren, Discovery of ZrCoBi based half Heuslers with high thermoelectric conversion efficiency, *Nat. Commun.* **9**, 2497 (2018).
- [15] C. Fu, S. Bai, Y. Liu, Y. Tang, L. Chen, X. Zhao, and T. Zhu, Realizing high figure of merit in heavy-band p-type half-Heusler thermoelectric materials, *Nat. Commun.* **6**, 8144 (2015).
- [16] K. Ciesielski, K. Synoradzki, I. Wolańska, P. Stachowiak, L. Kępiński, A. Jeżowski, T. Toliński, and D. Kaczorowski, High-temperature power factor of half-Heusler phases  $RENiSb$  ( $RE = Sc, Dy, Ho, Er, Tm, Lu$ ), *J. Alloys Compds.* **816**, 152596 (2020).
- [17] T. Harmening, H. Eckert, and R. Pöttgen, Defects in half-Heusler type antimonides  $ScTSb$  ( $T = Ni, Pd, Pt$ ), *Solid State Sci.* **11**, 900 (2009).
- [18] K. Synoradzki, K. Ciesielski, I. Veremchuk, H. Borrmann, P. Skokowski, D. Szymański, Y. Grin, and D. Kaczorowski, Thermal and electronic transport properties of the half-Heusler phase  $ScNiSb$ , *Materials* **12**, 1723 (2019).
- [19] K. Ciesielski, K. Synoradzki, I. Veremchuk, P. Skokowski, D. Szymański, Y. Grin, and D. Kaczorowski, Thermoelectric Performance of the half-Heusler Phases  $RENiSb$  ( $R = Sc, Dy, Er, Tm, Lu$ ): High Mobility Ratio between Majority and Minority Charge Carriers, *Phys. Rev. Appl.* **14**, 054046 (2020).
- [20] M. J. Winiarski, K. Bilińska, K. Ciesielski, and D. Kaczorowski, Thermoelectric performance of p-type half-heusler alloys  $ScMSb$  ( $M = Ni, Pd, Pt$ ) by ab initio calculations, *J. Alloys Compd.* **762**, 901 (2018).
- [21] I. Wolańska, K. Synoradzki, K. Ciesielski, K. Zaleski, P. Skokowski, and D. Kaczorowski, Enhanced thermoelectric power factor of half-Heusler solid solution  $Sc_{1-x}Tm_xNiSb$  prepared by high-pressure high-temperature sintering method, *Mater. Chem. Phys.* **227**, 29 (2019).
- [22] J. Oestreich, U. Probst, F. Richardt, and E. Bucher, Thermoelectrical properties of the compounds  $ScM^{VII}Sb$  and  $YM^{VIII}Sb$  ( $M^{VIII} = Ni, Pd, Pt$ ), *J. Physics: Condens. Matter* **15**, 635 (2003).
- [23] H. Hohl, A. P. Ramirez, W. Kaefer, K. Fess, C. Thurner, C. Kloc, and E. Bucher, A new class of materials with promising thermoelectric properties:  $MNiSn$  ( $M = Ti, Zr, Hf$ ), *MRS Proc.* **478**, 109 (1997).
- [24] H.-S. Kim, Z. M. Gibbs, Y. Tang, H. Wang, and G. J. Snyder, Characterization of lorenz number with seebeck coefficient measurement, *APL Mater.* **3**, 041506 (2015).

- [25] P. Price, Electronic thermal conduction in semiconductors, *Phys. Rev.* **95**, 596 (1954).
- [26] P. Price, Ambipolar thermodiffusion of electrons and holes in semiconductors, *Phil. Mag.* **46**, 1252 (1955).
- [27] J. R. Drabble and H. J. Goldsmid, *Thermal Conductivity in Semiconductors* (Pergamon Press, Inc., London, 1961), p. 104.
- [28] C. J. Glassbrenner and G. A. Slack, Thermal conductivity of silicon and germanium from 3K to the melting point, *Phys. Rev.* **134**, A1058 (1964).
- [29] L. D. Zhao, H. J. Wu, S. Q. Hao, C. I. Wu, X. Y. Zhou, K. Biswas, J. Q. He, T. P. Hogan, C. Uher, C. Wolverton, V. P. Dravid, and M. G. Kanatzidis, All-scale hierarchical thermoelectrics: MgTe in PbTe facilitates valence band convergence and suppresses bipolar thermal transport for high performance, *Energy Environ. Sci.* **6**, 3346 (2013).
- [30] W. Lu, S. Li, R. Xu, J. Zhang, D. Li, Z. Feng, Y. Zhang, and G. Tang, Boosting thermoelectric performance of SnSe via tailoring band structure, suppressing bipolar thermal conductivity, and introducing large mass fluctuation, *ACS Appl. Mater. Interfaces* **11**, 45133 (2019).
- [31] J.-H. Bahk and A. Shakouri, Enhancing the thermoelectric figure of merit through the reduction of bipolar thermal conductivity with heterostructure barriers, *Appl. Phys. Lett.* **105**, 052106 (2014).
- [32] Y. Xiao, H. Wu, J. Cui, D. Wang, L. Fu, Y. Zhang, Y. Chen, J. He, S. J. Pennycook, and L.-D. Zhao, Realizing high performance *n*-type PbTe by synergistically optimizing effective mass and carrier mobility and suppressing bipolar thermal conductivity, *Energy Environ. Sci.* **11**, 2486 (2018).
- [33] W. Fan, S. Chen, B. Zeng, Q. Zhang, Q. Meng, W. Wang, and Z. A. Munir, Enhancing the *zT* value of Bi-doped  $Mg_2Si_{0.6}Sn_{0.4}$  materials through reduction of bipolar thermal conductivity, *ACS Appl. Mater. Interfaces* **9**, 28635 (2017).
- [34] S. Foster and N. Neophytou, Effectiveness of nanojunctions for reducing bipolar effects in thermoelectric materials, *Comput. Mater. Sci.* **164**, 91 (2019).
- [35] H. Geng, X. Meng, H. Zhang, and J. Zhang, Lattice thermal conductivity of nanograined half-Heusler solid solutions, *Appl. Phys. Lett.* **104**, 202104 (2014).
- [36] S. Li, H. Zhao, D. Li, S. Jin, and L. Gu, Synthesis and thermoelectric properties of half-Heusler alloy YNiBi, *J. Appl. Phys.* **117**, 205101 (2015).
- [37] S. Chen, K. C. Lukas, W. Liu, C. P. Opeil, G. Chen, and Z. Ren, Effect of Hf concentration on thermoelectric properties of nanostructured *n*-type half-Heusler materials  $Hf_xZr_{1-x}NiSn_{0.99}Sb_{0.01}$ , *Adv. Energy Mater.* **3**, 1210 (2013).
- [38] J.-S. Rhyee, E. Cho, K. Ahn, K. H. Lee, and S. M. Lee, Thermoelectric properties of bipolar diffusion effect on  $In_4Se_{3-x}Te_x$  compounds, *Appl. Phys. Lett.* **97**, 152104 (2010).
- [39] H.-s. Kim, K. H. Lee, J. Yoo, J. Youn, J. W. Roh, S.-i. Kim, and S. W. Kim, Effect of substitutional Pb doping on bipolar and lattice thermal conductivity in *p*-type  $Bi_{0.48}Sb_{1.52}Te_3$ , *Materials* **10**, 763 (2017).
- [40] S. Wang, J. Yang, T. Toll, J. Yang, W. Zhang, and X. Tang, Conductivity-limiting bipolar thermal conductivity in semiconductors, *Sci. Rep.* **5**, 1 (2015).
- [41] K. Synoradzki, K. Ciesielski, L. Kępiński, and D. Kaczorowski, Power factor enhancement in a composite based on the half-heusler antimonide  $TmNiSb$ , *J. Appl. Phys.* **123**, 235101 (2018).
- [42] K. Synoradzki, K. Ciesielski, L. Kępiński, and D. Kaczorowski, Thermoelectric properties of  $(DyNiSn)_{1-x}(DyNiSb)_x$  composite, *Physica B* **536**, 659 (2018).
- [43] K. Ciesielski, D. Gnida, H. Borrmann, R. Ramlau, Y. Prots, D. Szymański, Y. Grin, and D. Kaczorowski, Structural, thermodynamic and magnetotransport properties of half-Heusler compound  $HoPtSb$ , *J. Alloys Compd.* **829**, 154467 (2020).
- [44] K. Synoradzki, K. Ciesielski, and D. Kaczorowski, Magnetocaloric effect in antiferromagnetic half-Heusler alloy  $DyNiSb$ , *Acta Phys. Pol. A* **133**, 691 (2018).
- [45] K. Ciesielski, K. Synoradzki, I. Wolańska, P. Stuglik, and D. Kaczorowski, High-temperature thermoelectric properties of half-Heusler phases  $Er_{1-x}Ho_xNiSb$ , *Mater. Today: Proc.* **8**, 562 (2019).
- [46] O. Pavloviuk, D. Kaczorowski, and P. Wiśniewski, Shubnikov-de Haas oscillations, weak antilocalization effect and large linear magnetoresistance in the putative topological superconductor  $LuPdBi$ , *Sci. Rep.* **5**, 9158 (2015).
- [47] O. Pavloviuk, D. Kaczorowski, and P. Wiśniewski, Superconductivity and Shubnikov-de Haas oscillations in the noncentrosymmetric half-Heusler compound  $YPtBi$ , *Phys. Rev. B* **94**, 035130 (2016).
- [48] B. Nowak, O. Pavloviuk, and D. Kaczorowski, Band inversion in topologically nontrivial half-Heusler bismuthides:  $209Bi$  NMR study, *J. Phys. Chem. C* **119**, 2770 (2015).
- [49] J. Rodriguez-Carvajal, Recent advances in magnetic structure determination by neutron powder diffraction, *Physica B* **192**, 55 (1993).
- [50] See Supplemental Material at <http://link.aps.org/supplemental/10.1103/PhysRevApplied.15.044047> for Figs. S1–S6 and Tables SI, SII.
- [51] T. Penkala, *Zarys Krystalografii* (Państw. Wydaw. Nauk., Warsaw, 1983).
- [52] H.-H. Xie, J.-L. Mi, L.-P. Hu, N. Lock, M. Chirstensen, C.-G. Fu, B. B. Iversen, X.-B. Zhao, and T.-J. Zhu, Interrelation between atomic switching disorder and thermoelectric properties of  $ZrNiSn$  half-Heusler compounds, *Cryst. Eng. Comm.* **14**, 4467 (2012).
- [53] W. G. Zeier, J. Schmitt, G. Hautier, U. Aydemir, Z. M. Gibbs, C. Felser, and G. J. Snyder, Engineering half-Heusler thermoelectric materials using Zintl chemistry, *Nat. Rev. Mater.* **1**, 1 (2016).
- [54] K. Gofryk, D. Kaczorowski, T. Plackowski, J. Mucha, A. Leithe-Jasper, W. Schnelle, and Y. Grin, Magnetic, transport, and thermal properties of the half-Heusler compounds  $ErPdSb$  and  $YPdSb$ , *Phys. Rev. B* **75**, 224426 (2007).
- [55] J. Mao, J. Shuai, S. Song, Y. Wu, R. Dally, J. Zhou, Z. Liu, J. Sun, Q. Zhang, C. dela Cruz, S. Wilson, Y. Pei, D. J. Singh, G. Chen, C.-W. Chu, and Z. Ren, Manipulation of ionized impurity scattering for achieving high thermoelectric performance in *n*-type  $Mg_3Sb_2$ -based materials, *Proc. Natl. Acad. Sci. U.S.A.* **114**, 10548 (2017).
- [56] K. Kishimoto, S. Koda, K. Akai, and T. Koyanagi, Thermoelectric properties of sintered type-II clathrates

- (K, Ba)<sub>24</sub>(Ga, Sn)<sub>136</sub> with various carrier concentrations, *J. Appl. Phys.* **118**, 125103 (2015).
- [57] Q. Ren, C. Fu, Q. Qiu, S. Dai, Z. Liu, T. Masuda, S. Asai, M. Hagihala, S. Lee, S. Torri, T. Kamiyama, L. He, X. Tong, C. Felser, D. J. Singh, T. Zhu, J. Yang, and J. Ma, Establishing the carrier scattering phase diagram for ZrNiSn-based half-Heusler thermoelectric materials, *Nat. Commun.* **11**, 3142 (2020).
- [58] J. Shuai, J. Mao, S. Song, Q. Zhu, J. Sun, Y. Wang, R. He, J. Zhou, G. Chen, D. J. Singh, and Z. Ren, Tuning the carrier scattering mechanism to effectively improve the thermoelectric properties, *Energy Environ. Sci.* **10**, 799 (2017).
- [59] H. Xie, H. Wang, C. Fu, Y. Liu, G. J. Snyder, X. Zhao, and T. Zhu, The intrinsic disorder related alloy scattering in ZrNiSn half-Heusler thermoelectric materials, *Sci. Rep.* **4**, 6888 (2014).
- [60] J. Schmitt, Z. M. Gibbs, G. J. Snyder, and C. Felser, Resolving the true band gap of ZrNiSn half-Heusler thermoelectric materials, *Mater. Horizons* **2**, 68 (2015).
- [61] H. J. Goldsmid and J. W. Sharp, Estimation of the thermal band gap of a semiconductor from Seebeck measurements, *J. Electron. Mater.* **28**, 869 (1999).
- [62] Z. M. Gibbs, H.-S. Kim, H. Wang, and G. J. Snyder, Band gap estimation from temperature dependent seebeck measurement – deviations from the  $2e | S_{\max} | T_{\max}$  relation, *Appl. Phys. Lett.* **106**, 022112 (2015).
- [63] H. J. Goldsmid, *Introduction to Thermoelectricity* (Springer, Berlin, 2010), Vol. 121.
- [64] C. Fu, M. Yao, X. Chen, L. Z. Maulana, X. Li, J. Yang, K. Imasato, F. Zhu, G. Li, and G. Auffermann *et al.*, Revealing the intrinsic electronic structure of 3D half-Heusler thermoelectric materials by angle-resolved photoemission spectroscopy, *Adv. Sci.* **7**, 1902409 (2020).
- [65] P. H. M. Böttger, G. S. Pomrehn, G. J. Snyder, and T. G. Finstad, Doping of *p*-type ZnSb: Single parabolic band model and impurity band conduction, *Phys. Status Solidi A* **208**, 2753 (2011).
- [66] G. A. Slack, *New Materials and Performance Limits for Thermoelectric Cooling* (CRC Press, Cleveland, 1995), p. 407.
- [67] G. J. Snyder, A. H. Snyder, M. Wood, R. Gurunathan, B. H. Snyder, and C. Niu, Weighted mobility, *Adv. Mater.* **32**, 2001537 (2020).
- [68] P. Graziosi and N. Neophytou, Ultra-high thermoelectric power factors in narrow gap materials with asymmetric bands, *J. Phys. Chem. C* **124**, 18462 (2020).
- [69] Y. Z. Pei, J. Yang, L. D. Chen, W. Zhang, J. R. Salvador, and J. Yang, Improving thermoelectric performance of caged compounds through light-element filling, *Appl. Phys. Lett.* **95**, 042101 (2009).
- [70] W. Liu, K. C. Lukas, K. McEnaney, S. Lee, Q. Zhang, C. P. Opeil, G. Chen, and Z. Ren, Studies on the Bi<sub>2</sub>Te<sub>3</sub>–Bi<sub>2</sub>Se<sub>3</sub>–Bi<sub>2</sub>S<sub>3</sub> system for mid-temperature thermoelectric energy conversion, *Energy Environ. Sci.* **6**, 552 (2013).
- [71] Y. Pei, A. D. LaLonde, H. Wang, and G. J. Snyder, Low effective mass leading to high thermoelectric performance, *Energy Environ. Sci.* **5**, 7963 (2012).
- [72] W. Ren, H. Geng, L. Zhang, X. Liu, T. He, and J. Feng, Simultaneous blocking of minority carrier and high energy phonon in *p*-type skutterudites, *Nano Energy* **46**, 249 (2018).
- [73] D. Narducci, Do we really need high thermoelectric figures of merit? A critical appraisal to the power conversion efficiency of thermoelectric materials, *Appl. Phys. Lett.* **99**, 102104 (2011).
- [74] R. He, G. Schierning, and K. Nielsch, Thermoelectric devices: A review of devices, architectures, and contact optimization, *Adv. Mater. Tech.* **3**, 1700256 (2018).
- [75] D. M. Rowe, *Materials, Preparation, and Characterization in Thermoelectrics* (CRC press, Taylor & Francis Group, Boca Raton, 2012), p. 11.
- [76] M. J. Winiarski and K. Bilińska, High thermoelectric power factors of *p*-type half-Heusler alloys YNiSb, LuNiSb, YPdSb, and LuPdSb, *Intermetallics* **108**, 55 (2019).
- [77] A. Jain, S. P. Ong, G. Hautier, W. Chen, W. D. Richards, S. Dacek, S. Cholia, D. Gunter, D. Skinner, and G. Ceder *et al.*, Commentary: The materials project: A materials genome approach to accelerating materials innovation, *APL Mater.* **1**, 011002 (2013).